Article:
Uddin, SZ and Talukder, MA orcid.org/0000-0002-2814-3658 (2017) Two-dimensional materials for improved resolution in total internal reflection fluorescence microscopy. Materials Research Express, 4 (9). 096203. ISSN 2053-1591

https://doi.org/10.1088/2053-1591/aa8a0f

Two-dimensional materials for improved resolution in total internal reflection fluorescence microscopy

Shiekh Zia Uddin[1] **and Muhammad Anisuzzaman Talukder**[1,2,*]

[1]*Department of Electrical and Electronic Engineering*

Bangladesh University of Engineering and Technology

Dhaka 1205, Bangladesh

[2]*School of Electronic and Electrical Engineering*

University of Leeds

Leeds LS2 9JT, United Kingdom

[*]*anis@eee.buet.ac.bd*

Abstract: We propose and theoretically demonstrate that two-dimensional materials at the interface between glass and water layers in a total internal reflection fluorescence microscopy (TIRFM) technique can decrease the detection volume of a target sample, and hence improve the resolution of the obtained image. In particular, we calculate the change in fluorescence characteristics of the fluorophore labels on a target sample when monolayer black phosphorus, hexagonal boron nitride, and graphene are added at the glass-water interface of a TIRFM structure. We also calculate the change in the detection volume due to the presence of two-dimensional materials, and when the polarization, wavelength, and angle of the incident light vary. We find $\gtrsim$10% and $\gtrsim$5% decrease in the detection volume when monolayer black phosphorus and hexagonal boron nitride are used, respectively, and up to $\sim$50% decrease when monolayer graphene is used. The proposed use of the two-dimensional material will significantly improve the resolution of TIRFM technique, and hence facilitate the study of nanoscale biological features.

1. Introduction

Total internal reflection fluorescence microscopy (TIRFM) is a technique to selectively excite fluorophore labels in a thin layer of a target sample and collect the emitted fluorescence of the excited fluorophores to create an image of the sample. Since, in TIRFM, the incident source light is totally reflected from the glass-water interface, and only the evanescent wave that decays exponentially

from the interface in the water region is used to excite the fluorophore labels, resolution of obtained images can be much better than that obtained using the techniques that are based on diffraction-limited optics [1,2]. Due to the fine resolution achieved using TIRFM, it is being used for imaging single molecules and studying in-vivo molecular dynamics [3–5]. However, although TIRFM can provide a resolution of < 200 nm, a better resolution is often necessary to study various nanoscale biological features, e.g., to study the topography of cell membrane to understand the interactions of cells with the surrounding environment.

In recent years, there has been a significant interest in atomically thin two-dimensional (2D) materials for their exciting electronic, optical, mechanical, and thermal properties [6–8]. For example, black phosphorus (BP) is a promising 2D material that can be exfoliated to only few layers and even to a monolayer [9]. In monolayer BP, the phosphorus atoms form a hexagonal lattice with a puckered structure resulting in in-plane anisotropic properties [10]. BP is being exploited for many potential applications including field effect transistors, heterojunction p-n diodes, photovoltaic devices, and photodetectors [11–14]. Another 2D material—monolayer hexagonal boron nitride (hBN)—has recently been isolated from bulk boron nitride, which is a layered material similar to graphite [15]. Monolayer hBN has also found widespread applications as a 2D dielectric substrate for graphene electronics [16–18]. It is also a natural hyperbolic material, and therefore, promises exciting and novel applications [19].

Among the 2D materials, graphene has drawn the most interest after being first discovered in 2004 [20]. Graphene has a unique property of conical band structure, which provides extraordinarily high mobility of carriers. Graphene also has many desired properties for robust and exciting applications—it is mechanically strong, chemically stable, and opto-electronically tunable. Therefore, it is not surprising that graphene has found rapid widespread applications across the

branches of science since its first demonstration in 2004. More recently, graphene is being explored for applications in photonics, optoelectronics, plasmonics, metamaterials, and biology [21–25]. Graphene also shows promises in improving the resolution in TIRFM when placed at the glass-water interface by selectively quenching the radiation of fluorophores that are close to the graphene layer [26]. The lifetimes of excited fluorophores on a target sample decrease significantly when the fluorophores are close to the graphene layer. In Ref. 26, the detection volume in TIRFM with a graphene layer at the glass-water interface was calculated and found to decrease up to $\sim$80 nm when the incidence angle varied for a fixed wavelength of light.

In this work, we theoretically show that 2D materials such as monolayer BP and hBN, in addition to graphene, at the interface between glass and water layers in a TIRFM structure are promising to decrease the detection volume. We develop theoretical models for each of BP, hBN, and graphene to calculate the detection volume when used at the glass-water interface in a TIRFM structure. In each case, we calculate the detection volume when the wavelength of fluorescence vary in the visible spectrum range and the angle of incident light vary beyond the critical angle. We find that the nonradiative dissipation of photons due to the interaction of fluorophores and nearby 2D material quenches the fluorescence from a region of the target sample that is close to the 2D material. The fluorescence quenching induced by monolayer BP, hBN, and graphene significantly decreases the thickness of the detection volume of a typical TIRFM technique, while without decreasing the fluorescence intensity. We find that the detection volume decreases irrespective of the angle of incidence and the polarization of the incident field. The detection volume decreases $\gtrsim 10\%$ and $\gtrsim 5\%$ when BP and hBN are used, respectively, and as much as $\sim$50% when graphene is used. The reduction in detection volume will improve the resolution of TIRFM and help to study various nanoscale biological features.

The rest of the paper is organized as follows: In Sec. 2, we present the structure that is usually used for TIRFM and the structure with the proposed use of a 2D material at the interface between glass and water layers. In Sec. 3, we develop theoretical approaches to calculate the detection volume in TIRFM when 2D materials are used at the glass-water interface. In Sec. 4, we present and discuss the detail dynamics obtained using the developed theoretical approaches in TIRFM with and without the 2D material at the the glass-water interface when the polarization, wavelength, and angle of incident light vary. In Sec. 5, we draw conclusions on the findings.

2. Proposed structure

In Fig. 1, we show schematic illustrations of structures for typical TIRFM and for TIRFM with the proposed 2D material at glass-water interface. The source light propagates through glass layer and is incident on the glass-water interface. Since the refractive index of glass is greater than that of water, i.e., $\varepsilon_p > \varepsilon_w$, the incident light is totally reflected if the angle of incidence is greater than the critical angle. Although the incident light is reflected from the glass-water interface, an evanescent field exponentially decays in water. If fluorescently-labeled samples are placed close to the interface, the fluorophores from a thin layer can be excited. Since the excited fluorophores radiate light at a longer wavelength than that with which they are excited, the radiation from the excited fluorophores can be collected in the glass side and converted to microscopy image using appropriate optical arrangements [3]. In Fig. 1(b), for the structure with monolayer BP, hBN, or graphene at the glass-water interface, the target sample with fluorophore labels will be placed in water near the 2D material. The excitation and collection schemes used in a typical TIRFM technique can be used for the proposed structure. The excited fluorophores on the target sample that are close to the 2D material will be quenched, and hence the effective volume of the target

sample from where the fluorophore radiation is collected will decrease.

3. Theoretical modeling

3.1. Optical properties of 2D materials

A 2D material is optically anisotropic with a permittivity tensor given by [27]

$$\overleftrightarrow{\varepsilon} = \begin{bmatrix} \varepsilon_{xx} & 0 & 0 \\ 0 & \varepsilon_{yy} & 0 \\ 0 & 0 & \varepsilon_{zz} \end{bmatrix}, \tag{1}$$

where ε_{xx} and ε_{yy} are the relative permittivities in the directions of in-plane principal axes and ε_{zz} is the relative permittivity in the vertical direction. The relative permittivity in the direction of any of the principal axes can be written as [28]

$$\varepsilon_{jj} = \varepsilon_j^{\infty} + \frac{i\sigma_{jj}}{\varepsilon_0 \omega a}, \tag{2}$$

where $j = x, y, z$ denotes the directions, ε_j^{∞} is the relative permittivity at a very high frequency in the j-direction, σ_{jj} is the optical conductivity in the j-direction, and a is the thickness of the 2D material. Due to the 2D nature of the material, the electric field that is polarized in the normal direction to the material cannot excite any current. Therefore, the normal component of the surface conductivity σ_{zz} is assumed to be zero [29].

Black Phosphorus

The in-plane conductivity of 2D monolayer BP is given by [30]

$$\sigma_{jj} = \frac{ie^2 n}{m_j(\omega + i\eta/\hbar)}, \tag{3}$$

where m_j is the electron effective mass in the j-direction, η is the relaxation rate, n is the electron doping density, and $\hbar$ is the reduced Planck's constant. We calculate the in-plane σ_{jj} of monolayer BP using the parameter values given in Table 1. The in-plane relative permittivities are calculated using Eq. (2). We show the real parts of in-plane relative permittivities of monolayer BP in Fig. 2(a) for visible wavelength range of the incident light. We note that while $\mathrm{Re}(\varepsilon_{xx})$ does not change with the wavelength of the incident light, $\mathrm{Re}(\varepsilon_{yy})$ decreases gradually as the wavelength increases. The imaginary parts of in-plane relative permittivities of monolayer BP are approximately two orders of magnitude smaller than the real parts, and therefore, are not shown here.

Hexagonal Boron Nitride

Although Eq. (2) is a widely used model to calculate permittivities of many 2D materials, including monolayer BP and graphene, the permittivities of monolayer hBN are often modeled using a single Lorentzian from as [31]

$$\varepsilon_{jj} = \varepsilon_j^{\infty}\left(1 - \frac{\omega_{\mathrm{LO},j}^2 - \omega_{\mathrm{TO},j}^2}{\omega^2 + i\omega\gamma_j - \omega_{\mathrm{TO},j}^2}\right), \tag{4}$$

where ω_{LO}, ω_{TO} represent the longitudinal and transverse optical phonon frequencies, respectively, and γ_j represents the damping constant. We calculate in-plane relative permittivities of monolayer hBN using the parameter values given in Table 1. We show the real parts of in-plane relative permittivities of hBN in Fig. 2(b) for visible wavelength range of the incident light. We note that

the real parts of relative permittivities in the directions of in-plane principal axes are equal, i.e., $\mathrm{Re}(\varepsilon_{xx}) = \mathrm{Re}(\varepsilon_{yy})$, and do not change with the wavelength of the incident light. The imaginary parts of in-plane relative permittivities of hBN are approximately nine orders of magnitude smaller than the real parts, and therefore, are not shown here.

Graphene

The optical response model of graphene considers it as an ultra-thin two-sided surface characterized by a conductivity $\sigma(\omega, \mu_c, \Gamma, T)$, which depends on the angular frequency ω, chemical potential μ_c, phenomenological scattering rate Γ, and temperature T. Graphene's complex conductivity can be determined using the Kubo formula [28]

$$\sigma_{xx} = \sigma_{yy} = \sigma(\omega, \mu_c, \Gamma, T) = \sigma_{\text{intra}}(\omega, \mu_c, \Gamma, T) + \sigma_{\text{inter}}(\omega, \mu_c, \Gamma, T), \tag{5}$$

where σ_{intra} and σ_{inter} are the intra-band and inter-band conductivities, respectively. The intra-band contribution can be written as

$$\sigma_{\text{intra}}(\omega, \mu_c, \Gamma, T) = i\frac{1}{\pi\hbar^2}\frac{e^2 k_B T}{(\omega + 2i\Gamma)}\left\{\frac{\mu_c}{k_B T} + 2\ln\left[\exp\left(-\frac{\mu_c}{k_B T}\right) + 1\right]\right\}, \tag{6}$$

and the inter-band contribution can be approximated for $\mu_c >> k_B T$ as

$$\sigma_{\text{inter}}(\omega, \mu_c, \Gamma, T) = i\frac{e^2}{4\pi\hbar}\ln\left[\frac{2|\mu_c| - \hbar(\omega + 2i\Gamma)}{2|\mu_c| - \hbar(\omega + 2i\Gamma)}\right], \tag{7}$$

where e is the electronic charge and k_B is the Boltzmann constant [32].

The chemical potential μ_c can be tuned by the application of a transverse voltage, electric field,

magnetic field, and chemical doping. Typically, μ_c can be varied from zero to 1 eV. We calculate the in-plane conductivities of graphene using the parameter values given in Table 1. The in-plane relative permittivities of graphene are calculated using Eq. (2). We show the real and imaginary parts of the relative permittivities of graphene in Fig. 2(c) for visible wavelength range of the incident light. We note that $\varepsilon_{xx} = \varepsilon_{yy}$ for graphene and both the real and imaginary parts of relative permittivities increase as the wavelength of the incident light increases.

3.2. Total internal reflection

The critical angle for an incident wave from glass on a glass-water planar interface is $\theta_c = \sin^{-1}\left(\sqrt{\varepsilon_w/\varepsilon_p}\right)$. If a wave is incident at an angle $\theta_i > \theta_c$, the transmitted wave in water decays exponentially with the distance from the interface irrespective of the polarization and wavelength of the incident wave. For a planar structure, the evanescent electric field in water due to p-polarized incident light can be written as [33]

$$\mathbf{E_p} = E_0 t_p (\hat{\mathbf{x}}\sqrt{\varepsilon_p \sin^2\theta_i - \varepsilon_w} + j\hat{\mathbf{z}}\sqrt{\varepsilon_p}\sin\theta_i)\exp(-z/2d), \tag{8}$$

and the evanescent electric field in water due to s-polarized incident light can be written as

$$\mathbf{E_s} = E_0 t_s \hat{\mathbf{y}}\exp(-z/2d), \tag{9}$$

where $d = (\lambda/4\pi)\sqrt{\varepsilon_p \sin^2(\theta_i) - \varepsilon_w}$ is the penetration depth, E_0 is the amplitude of the incident light, and t_p and t_s are the Fresnel transmission coefficients for p- and s-polarized light, respectively. We note that the evanescent electric fields $\mathbf{E_p}$ and $\mathbf{E_s}$ excite the fluorophore labels on the target sample in TIRFM, and generally, we can denote them as $\mathbf{E_{ex}}$. In this work, we calculate the

Fresnel coefficients of the anisotropic glass-2D material-water media using the 4×4 transfer matrix method described in Refs. 34 and 35.

3.3. Fluorescence near planar stratified media

If the fluorophore labels on the target sample are excited by the evanescent field $\mathbf{E_{ex}}$, they absorb the excitation light at a resonant wavelength. Subsequently, the fluorophore labels emit the absorbed energy, however, at a longer wavelength. The emitted energy can be collected either in the glass side or in the water side using appropriate optical arrangements [33]. If the fluorophores are randomly oriented on the target sample, then the collected fluorescence at a specific point on the *x*-*y* plane will depend on the fluorophore density distribution $C(z)$ in the z-direction. The collected fluorescence intensity from a pixel (x,y) near a planar interface can be written as [33, 36]

$$F = k \int dz\, C(z)[w^{\perp}(z)Q^{\perp}(z) + w^{\parallel}(z)Q^{\parallel}(z)] = k \int dz\, C(z)g(z), \tag{10}$$

where k is a proportionality constant consisting of conversion factors, and normalization and arithmetic constants, $w^{\perp,\parallel}(z)$ are the weighting terms, and $Q^{\perp,\parallel}(z)$ are the collection efficiencies for vertical and horizontal dipoles. The weighting terms represent the amount of horizontal and vertical dipoles excited by the excitation light $\mathbf{E_{ex}}$, which depend on the local orientation of the dipole and the polarization of the incident light. The function $g(z) = [w^{\perp}(z)Q^{\perp}(z) + w^{\parallel}(z)Q^{\parallel}(z)]$ selects the region of the target sample in the vertical direction that contributes to the collected fluorescence intensity.

The total rate of energy dissipation (P) by an excited fluorophore placed near a planar interface

normalized by that of a fluorophore placed in vacuum (P_0) can be numerically calculated by [33]

$$\frac{P}{P_0} = 1 + \frac{3}{4}\sin^2\beta \int_0^\infty \mathrm{Re}\left[\frac{s}{\sqrt{1-s^2}}\left(r_s - (1-s^2)r_p\right)e^{2ik_1 z\sqrt{1-s^2}}\right] ds + \frac{3}{2}\cos^2\beta \int_0^\infty \mathrm{Re}\left[\frac{s^3}{\sqrt{1-s^2}} r_p e^{2ik_1 z\sqrt{1-s^2}}\right] ds, \tag{11}$$

where β is the angle that the fluorophore dipole moment makes with the z-axis, r_s and r_p are the Fresnel reflection coefficients for the p- and s-polarized incident light, $k_1 = 2\pi\sqrt{\varepsilon_w}/\lambda$ is the wavevector in water, and z is the height of the fluorophore from the nearest interface. As the normalized rate of energy dissipation is identical to the normalized spontaneous decay rate of a quantum-mechanical two-level system such as a fluorophore, the normalized lifetime $\tau/\tau_0 = P_0/P$ [37]. The lifetime of a fluorophore is not only a function of the structure of the atom but also of the surrounding environment. The surrounding environment changes both photon emission and nonradiative decay rates of a fluorophore. The nonradiative decay rate of a fluorophore when placed near a metallic surface increases significantly, so that the excited state lifetime becomes almost zero, which is often called fluoroscence quenching [33]. The lifetimes of horizontal and vertical fluorophores emitting photons at wavelength λ and placed at height z from the interface of water and glass in a typical TIRFM structure or from the interface of water and 2D material such as monolayer BP, hBN, and graphene in the proposed TIRFM structure are shown in Fig. 3. We note that when z is small, i.e., $z \lesssim 30$ nm, the excited state lifetime of fluorophores decreases significantly with the use of a 2D material compared to that when there is no 2D material as in a typical TIRFM structure.

The normalized power radiated into glass by a fluorophore placed at height z can be calculated

by [33]

$$\frac{P_g}{P_0} = \frac{3\sqrt{\varepsilon_w}}{8\sqrt{\varepsilon_g}} \sin^2\beta \int_0^{\sqrt{\varepsilon_g/\varepsilon_w}} s\sqrt{1-\frac{\varepsilon_w}{\varepsilon_g}s^2}\left[|t_p|^2 + \frac{|t_s|^2}{|1-s^2|}\right] e^{-2k_1 z s_z'} ds$$
$$+ \frac{3\sqrt{\varepsilon_w}}{4\sqrt{\varepsilon_g}} \cos^2\beta \int_0^{\sqrt{\varepsilon_g/\varepsilon_w}} s^3\sqrt{1-\frac{\varepsilon_w}{\varepsilon_g}s^2}\frac{|t_p|^2}{|1-s^2|} e^{-2k_1 z s_z'} ds, \tag{12}$$

where $s_z' = \mathrm{Im}\left[\sqrt{1-s^2}\right]$. The parameter values $\beta = 0$ and $\beta = \pi/2$ represent vertical and horizontal fluorophores, respectively. Collection efficiency is the ratio of fluorescence energy collected by the imaging system to that total emitted by the excited fluorophores. Collection efficiency depends on the position, orientation, and environment of the fluorophore and can be calculated as

$$Q^{\perp} = \left.\frac{P_g}{P}\right|_{\beta=0}, \; Q^{\parallel} = \left.\frac{P_g}{P}\right|_{\beta=\pi/2}. \tag{13}$$

The collection efficiencies for horizontal and vertical fluorophores emitting photons at wavelength λ and placed at height z from the interface of water and glass in a typical TIRFM structure or from the interface of water and 2D material such as monolayer BP, hBN, and graphene in the proposed TIRFM structure are shown in Fig. 4. We note that if the fluorophore is placed near the 2D material, the collected fluorescence decreases significantly compared to that in the typical TIRFM structure as fluorophores are nonradiatively quenched by the nearby 2D material.

If $\mathbf{E_{ex}} = \hat{\mathbf{x}}E_{ex}^x + \hat{\mathbf{y}}E_{ex}^y + \hat{\mathbf{z}}E_{ex}^z$ is the phasor representation of the excitation electric field, then the weighting terms can be written as

$$w^{\perp,\parallel}(z) = |E_{ex}^x|^2 w_x^{\perp,\parallel}(z) + |E_{ex}^y|^2 w_y^{\perp,\parallel}(z) + |E_{ex}^z|^2 w_z^{\perp,\parallel}(z). \tag{14}$$

The detail forms of the function $w_{x,y,z}^{\perp,\parallel}(z)$ are given in Ref. 36. The weighting functions depend on lifetime ratio $\eta(z) = \tau^{\perp}(z)/\tau^{\parallel}(z)$, where $\tau^{\parallel}(z)$ and $\tau^{\perp}(z)$ are the lifetimes of horizontal and vertical dipoles situated at height z.

4. Results

The function $g(z)$ selects the region of the sample where the fluorophores are excited to emit light to effectively contribute to the collected fluorescence. We calculate $g(z)$ for a typical TIRFM technique and the proposed TIRFM technique with a 2D material using the theoretical approach described in this paper. We vary the wavelength, incidence angle, and polarization of the incident light. Figure 5 shows $g(z)$ with varying incidence angle at a wavelength $\lambda = 565$ nm. Figures 5(a) and 5(b) show $g(z)$ for p- and s-polarized excitation field for the typical TIRFM structure. We note that $g(z)$ decreases with height z from the glass-water interface irrespective of the incidence angle primarily due to the exponential decay of the excitation field. The function $g(z)$ in the glass-graphene-water structure at $\lambda = 565$ nm is shown in Figs. 5(c) and 5(d) for p- and s-polarized excitations, respectively. We note that, for a region close to the interface, $g(z)$ is smaller in Figs. 5(c) and 5(d) than that in Figs. 5(a) and 5(b) due to the quenching of fluorophores by the graphene layer. The quenching of fluorescence decreases the effective volume of the target sample excited by both the p- and s-polarized field. The amplitude levels of $g(z)$, which represent the fluorescence intensity at collection, are similar in the typical TIRFM structure and in the proposed TIRFM structure with a 2D graphene layer.

We calculate the full-width at half-maximum (FWHM) of $g(z)$ to determine the thickness of the detection volume in the z-direction in the visible wavelength range. Figures 6(a) and 6(b) show the thickness of detection volume obtained using a typical TIRFM structure for p- and s-

polarized light for varying wavelength and incidence angle. For the three 2D materials discussed here, we achieve a significant decrease in the thickness of the detection volume so that the decrease $\Delta^{p,s}_{BP,hBN,G} = \delta^{p,s}_{B} - \delta^{p,s}_{BP,hBN,G} \gg 0$, where $\delta^{p,s}_{BP,hBN,G}$ is the detection volume thickness for p- and s-polarized light with BP, hBN, and graphene, and $\delta^{p,s}_{B}$ is the detection volume thickness in a typical TIRFM technique. Figures 6(c) and 6(d) show Δ_{BP} for p- and s-polarized excitation achieved by the presence of a monolayer BP film at the glass-water interface. We note that the use of monolayer BP achieves a polarization independent $\sim$30 nm decrease in the FWHM thickness of $g(z)$, which is $\gtrsim$10% decrease of the detection volume. Figures 6(e) and 6(f) show Δ_{hBN} for p- and s-polarized excitation achieved by the presence of a monolayer hBN film at the glass-water interface. We note that the use of monolayer hBN achieves a polarization independent $\sim$20 nm decrease in the FWHM of $g(z)$. Figures 6(g) and 6(h) show Δ_{G} for p- and s-polarized excitation achieved by the presence of a monolayer graphene film at the glass-water interface. We note that the use of monolayer graphene achieves a maximum of $\sim$120 nm decrease in the FWHM thickness, which is $\sim$50% decrease of the detection volume.

5. Conclusion

In conclusion, we proposed and theoretically demonstrated that 2D materials monolayer BP, hBN, and graphene at the glass-water interface can decrease the detection volume in TIRFM so that the resolution of microscopy images can be improved. We developed theoretical approaches to calculate the detection volume when BP, hBN, and graphene are used at the glass-water interface of a TIRFM structure. In each case, we found that the detection volume decreases significantly without decreasing the fluorescence intensity irrespective of the polarization, wavelength, and angle of the incident light. The detection volume in TIRFM decreases $\gtrsim$ 10% and $\gtrsim$ 5% when monolayer BP

and hBN are used, respectively, and as much as $\sim 50\%$ when monolayer graphene is used.

References

1. D. Axelrod, Methods Cell Biol **30**, 245–270 (1989).
2. D. Axelrod, E. H. Hellen, and R. M. Fulbright, "Total internal reflection fluorescence," in "Topics in fluorescence spectroscopy," (Springer, 2002), pp. 289–343.
3. A. L. Mattheyses, S. M. Simon, and J. Z. Rappoport, J. Cell Science **123**, 3621–3628 (2010).
4. D. S. Johnson, J. K. Jaiswal, and S. Simon, Current Protocols in Cytometry **12**, 12–29 (2012).
5. D. Axelrod, Traffic **2**, 764–774 (2001).
6. F. Xia, H. Wang, D. Xiao, M. Dubey, and A. Ramasubramaniam, Nature Photonics **8**, 899–907 (2014).
7. G. Fiori, F. Bonaccorso, G. Iannaccone, T. Palacios, D. Neumaier, A. Seabaugh, S. K. Banerjee, and L. Colombo, Nature Nanotechnology **9**, 768–779 (2014).
8. X. Ling, H. Wang, S. Huang, F. Xia, and M. S. Dresselhaus, Proceedings of the National Academy of Sciences **112**, 4523–4530 (2015).
9. A. Castellanos-Gomez, L. Vicarelli, E. Prada, J. O. Island, K. Narasimha-Acharya, S. I. Blanter, D. J. Groenendijk, M. Buscema, G. A. Steele, and J. Alvarez, 2D Materials **1**, 025001 (2014).
10. J. Qiao, X. Kong, Z.-X. Hu, F. Yang, and W. Ji, Nature Communications **5** (2014).
11. L. Li, Y. Yu, G. J. Ye, Q. Ge, X. Ou, H. Wu, D. Feng, X. H. Chen, and Y. Zhang, Nature Nanotechnology **9**, 372–377 (2014).
12. S. P. Koenig, R. A. Doganov, H. Schmidt, A. Castro Neto, and B. Özyilmaz, Applied Physics Letters **104**, 103106 (2014).

13. M. Buscema, D. J. Groenendijk, S. I. Blanter, G. A. Steele, H. S. van der Zant, and A. Castellanos-Gomez, Nano Letters **14**, 3347–3352 (2014).

14. R. Fei and L. Yang, Nano Letters **14**, 2884–2889 (2014).

15. L. Song, L. Ci, H. Lu, P. B. Sorokin, C. Jin, J. Ni, A. G. Kvashnin, D. G. Kvashnin, J. Lou, and B. I. Yakobson, Nano Letters **10**, 3209–3215 (2010).

16. J. Xue, J. Sanchez-Yamagishi, D. Bulmash, P. Jacquod, A. Deshpande, K. Watanabe, T. Taniguchi, P. Jarillo-Herrero, and B. J. LeRoy, Nature Materials **10**, 282–285 (2011).

17. W. Yang, G. Chen, Z. Shi, C.-C. Liu, L. Zhang, G. Xie, M. Cheng, D. Wang, R. Yang, and D. Shi, Nature Materials **12**, 792–797 (2013).

18. C. R. Dean, A. F. Young, I. Meric, C. Lee, L. Wang, S. Sorgenfrei, K. Watanabe, T. Taniguchi, P. Kim, and K. L. Shepard, Nature Nanotechnology **5**, 722–726 (2010).

19. S. Dai, Q. Ma, M. Liu, T. Andersen, Z. Fei, M. Goldflam, M. Wagner, K. Watanabe, T. Taniguchi, and M. Thiemens, Nature Nanotechnology **10**, 682–686 (2015).

20. K. S. Novoselov, A. K. Geim, S. Morozov, D. Jiang, Y. Zhang, S. Dubonos, , I. Grigorieva, and A. Firsov, Science **306**, 666–669 (2004).

21. F. Bonaccorso, Z. Sun, T. Hasan, and A. Ferrari, Nature Photonics **4**, 611–622 (2010).

22. C.-H. Liu, Y.-C. Chang, T. B. Norris, and Z. Zhong, Nature Nanotechnology **9**, 273–278 (2014).

23. A. Grigorenko, M. Polini, and K. Novoselov, Nature Photonics **6**, 749–758 (2012).

24. M. A. Othman, C. Guclu, and F. Capolino, Optics Express **21**, 7614–7632 (2013).

25. K. Kostarelos and K. S. Novoselov, Science **344**, 261–263 (2014).

26. S. Z. Uddin and M. A. Talukder, in Proc. in *International Conference on Electrical and*

Computer Engineering, (ICECE, 2016), pp. 143–146.

27. A. Nemilentsau, T. Low, and G. Hanson, Physical Review Letters **116**, 066804 (2016).
28. L. Falkovsky and S. Pershoguba, Physical Review B **76**, 153410 (2007).
29. B. Zhu, G. Ren, S. Zheng, Z. Lin, and S. Jian, Optics Express **21**, 17089–17096 (2013).
30. T. Low, R. Roldán, H. Wang, F. Xia, P. Avouris, L. M. Moreno, and F. Guinea, Physical Review Letters **113**, 106802 (2014).
31. Y. Cai, L. Zhang, Q. Zeng, L. Cheng, and Y. Xu, Solid State Communications **141**, 262–266 (2007).
32. G. W. Hanson, J. Applied Physics **103**, 064302 (2008).
33. L. Novotny and B. Hecht, *Principles of Nano-optics* (Cambridge university press, 2012).
34. D. W. Berreman, J. Optical Society of America **62**, 502–510 (1972).
35. M. Schubert, Physical Review B **53**, 4265 (1996).
36. E. H. Hellen and D. Axelrod, J. Optical Society of America B **4**, 337–350 (1987).
37. L. Novotny, Applied Physics Letters **69**, 3806–3808 (1996).
38. Z. Liu and K. Aydin, Nano Letters **16**, 3457–3462 (2016).
39. T. Low, A. Rodin, A. Carvalho, Y. Jiang, H. Wang, F. Xia, and A. C. Neto, Physical Review B **90**, 075434 (2014).
40. N. Ohba, K. Miwa, N. Nagasako, and A. Fukumoto, Physical Review B **63**, 115207 (2001).
41. A. Vakil and N. Engheta, Science **332**, 1291–1294 (2011).

Tables and Figures

Table 1: Key parameter values for monolayer BP, hBN, and graphene

2D Material	Parameter	Value
BP [38, 39]	m_x	$0.0421m_e$
	m_y	$0.7m_e$
	n	10^{13} cm^{-2}
	η	10 meV
	a	1 nm
	$\varepsilon_x^\infty = \varepsilon_y^\infty = \varepsilon_z^\infty$	5.76
hBN [40]	$\varepsilon_x^\infty = \varepsilon_y^\infty$	2.84
	ε_z^∞	4.85
	$\gamma_x = \gamma_y$	2.35×10^{11} Hz
	γ_z	2.345×10^{11} Hz
	$\omega_{\mathrm{TO},x} = \omega_{\mathrm{TO},y}$	2.4999×10^{15} Hz
	$\omega_{\mathrm{LO},x} = \omega_{\mathrm{LO},y}$	2.2903×10^{15} Hz
	$\omega_{\mathrm{TO},z}$	1.3639×10^{15} Hz
	$\omega_{\mathrm{LO},z}$	1.1679×10^{15} Hz
Graphene [41]	Γ	0.1 meV
	μ_c	0.7 meV
	$\varepsilon_x^\infty = \varepsilon_y^\infty = \varepsilon_z^\infty$	1
	a	0.364 nm

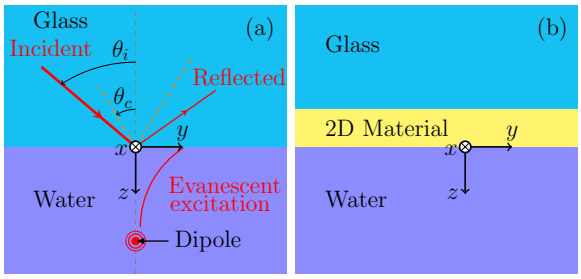

Fig. 1: (a) Schematic illustration of a typical TIRFM structure where a glass-water interface is used to generate the evanescent excitation wave and (b) proposed TIRFM structure where a 2D material is placed at the glass-water interface.

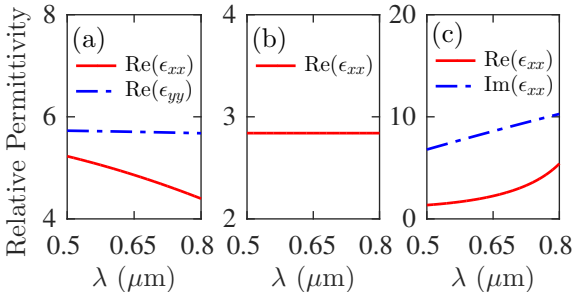

Fig. 2: Relative permittivities of (a) BP, (b) hBN, and (c) graphene for varying wavelength (λ). For hBN, $\mathrm{Re}(\varepsilon_{xx}) = \mathrm{Re}(\varepsilon_{yy})$.

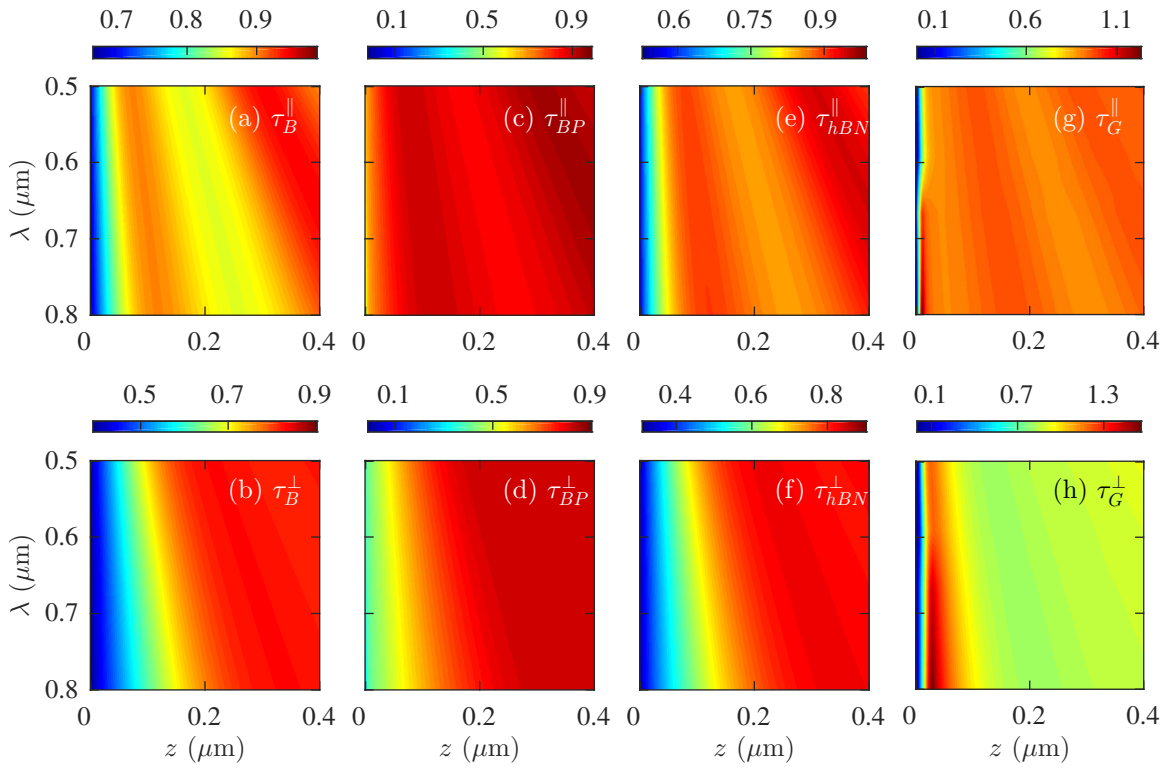

Fig. 3: Lifetimes of horizontal and vertical fluophores for varying wavelength (λ) and height (z) in (a,b) typical TIRFM structure, and in TIRFM structure with (c,d) BP, (e,f) hBN, and (g,h) graphene.

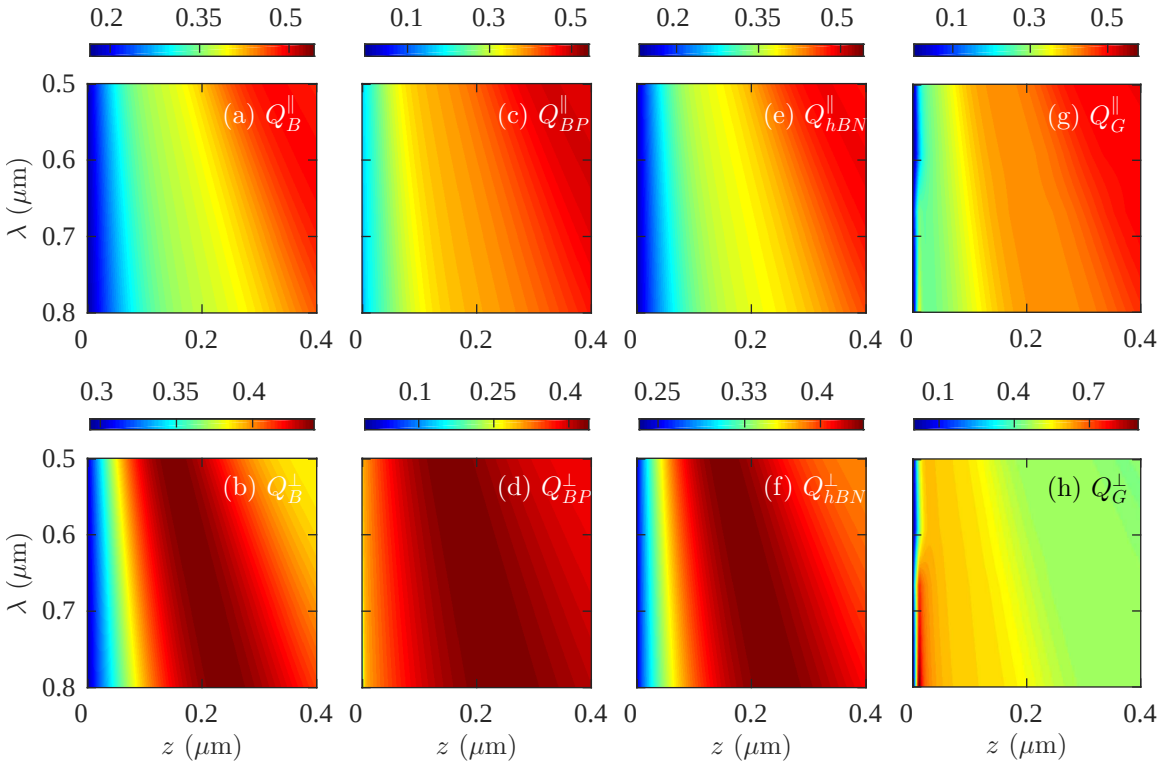

Fig. 4: Collection efficiencies of horizontal and vertical fluophores for varying wavelength (λ) and height (z) in (a,b) typical TIRFM structure, and in TIRFM structure with (c,d) BP, (e,f) hBN, and (g,h) graphene.

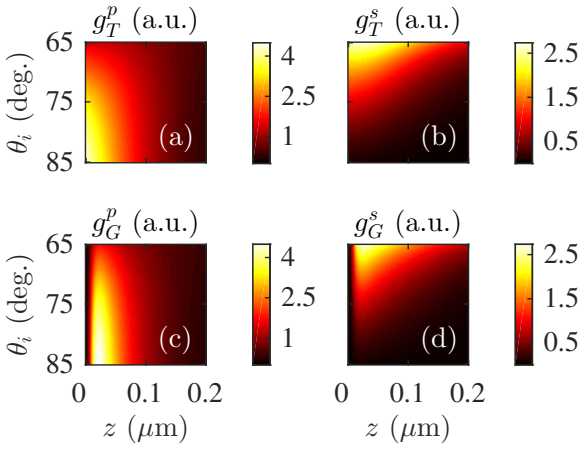

Fig. 5: Function $g(z)$ with varying incidence angle (θ_i) and height (z) in a typical TIRFM structure when the incident light is (a) p- and (b) s-polarized. Function $g(z)$ with varying incidence angle (θ_i) and height (z) in the proposed TIRFM structure with monolayer graphene when the incident light is (c) p- and (d) s-polarized. In each case, the wavelength of the incident light $\lambda = 565$ nm.

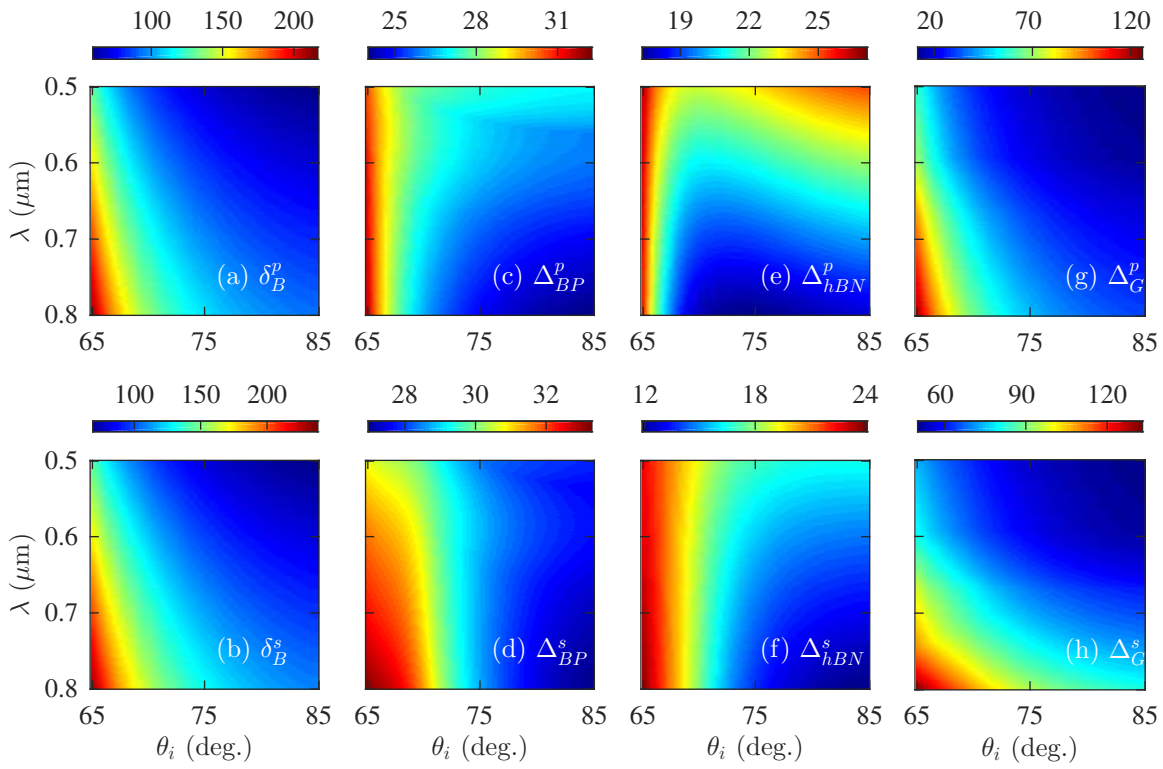

Fig. 6: Detection volume of horizontal and vertical fluophores for varying wavelength (λ) and height (z) in (a,b) typical TIRFM structure, and decrease in detection volume thickness with (c,d) BP, (e,f) hBN, and (g,h) graphene for p- and s-polarized light.